THE ASTROPHYSICAL JOURNAL, 440:241–253, 1995 February 10

GAS PHASE ABUNDANCES AND CONDITIONS ALONG THE SIGHT LINE TO THE LOW-HALO, INNER GALAXY STAR HD 167756[1]

JASON A. CARDELLI,[2,3] KENNETH R. SEMBACH,[4] AND BLAIR D. SAVAGE[2]

Received 1994 June 2; accepted 1994 August 18

ABSTRACT

We present high-resolution (3.5 km s^{-1}) Goddard High Resolution Spectrograph (GHRS) measurements of the Mg II, Si II, Cr II, Fe II, and Zn II lines toward HD 167756, a low-latitude halo star at a distance of 4 kpc in the direction $l = 351.°5$, $b = -12.°3$ and at a Galactic altitude of $z = -0.85$ kpc. Supplemental Na I, Ca II, and H I data are also presented for comparison with the UV lines. Our analysis centers on converting the observed absorption-line data into measures of the apparent column density per unit velocity, $N_a(v)$, over the velocity range $-25 \leq v_{lsr} < 30$ km s^{-1} for each species observed. We use these $N_a(v)$ profiles to construct logarithmic abundance ratios of Mg II, Si II, Cr II, Fe II, and Ca II relative to Zn II, normalized to solar abundances, as a function of velocity. Compared to Zn, these species show an underabundance relative to their solar values, with the largest underabundances occurring in the $v_{lsr} \approx 5$ km s^{-1} component(s), for which we find logarithmic abundances $A_{Si/Zn} > -0.38$, $A_{Mg/Zn} = -0.82$, $A_{Cr/Zn} = -1.18$, and $A_{Fe/Zn} > -1.40$ dex. We show that ionization effects, abundance gradients, or intrinsic abundance variability cannot be significant sources for the underabundances observed. The most likely explanation is gas phase depletion of elements onto dust grains. Comparisons with the gas phase abundances along other diffuse, warm gas sight lines, like the halo sight line to HD 93521, support this interpretation as do the derived physical properties of the sight line.

We find that the sight line to HD 167756 is characterized by warm, low-density gas interspersed with several zones of higher density, cooler gas. The gas temperatures of the neutral regions containing the observed dominant ion absorption are probably between 1000 and 5000 K (our analysis includes temperatures as high as 7000 K if Na is undepleted), although some clouds, particularly those detected in Na I, may have $T < 1000$ K. The electron densities determined from ionization balance considerations are $0.02 < n_e < 0.20$ cm^{-3}. This range, more typical of denser molecule-bearing clouds, probably signifies mixing between strictly neutral gas and gas containing H^+. Differences arising in the physical properties like temperature and n_e determined from species such as Na I or Zn II and Ca II can be explained if some of the low ion absorption occurs in transition regions between neutral and ionized gas. Structured absorption seen in more highly ionized species like Si IV and C IV favors the existence of such regions along the sight line.

Subject headings: ISM: abundances — stars: individual (HD 167756) — ultraviolet: ISM

1. INTRODUCTION

The detailed study of neutral interstellar gas through analysis of atomic absorption lines arising from neutral and dominant ions provides important information on the physical conditions, structure, and elemental abundances of interstellar clouds. Most of these studies have concentrated on lightly reddened, nearby sight lines or relatively reddened [$E(B-V) > 0.15$] sight lines within 2 kpc (Jenkins, Savage, & Spitzer 1986) that typically sample moderately dense gas ($n \geq 200$ cm^{-3}). However, comparatively little is known about the characteristics of neutral (H I) gas in large Galactic distances, especially in low-mass diffuse clouds characterized by relatively low density ($n \ll 200$ cm^{-3}). Extended sight lines are important because they provide the opportunity to study gas and dust characteristics on a Galactic scale, including such effects as abundance gradients.

In this paper we explore the neutral gas characteristics in the sight line toward HD 167756, a lightly reddened [$E(B-V) = 0.09$] B0.5 Ia star located in the general direction of the Galactic center ($l = 351.°5$, $b = -12.°3$) at a distance of about 4 kpc from the Sun and at a Galactic altitude of $z = -0.85$ kpc. The data analyzed here consist of UV atomic absorption lines of Mg II, Si II, Cr II, Fe II, and Zn II obtained with the high-dispersion (3.5 km s^{-1} resolution) echelle gratings of the Goddard High Resolution Spectrograph (GHRS). (This paper represents a companion study to that of Savage, Sembach, & Cardelli [1994], which discusses the characteristics of the highly ionized gas toward HD 167756 through the analysis of absorption lines of Si IV, C IV, and N V obtained with the GHRS.) The atomic species/lines studied here exhibit absorption principally over -25 km $s^{-1} \leq v_{lsr} < 30$ km s^{-1}, and we restrict our discussion to this velocity range, although weaker low ion atomic absorption can be traced out to -40 and $+60$ km s^{-1}.

2. OBSERVATIONS AND REDUCTION

We obtained observations of various inerstellar absorption lines in the spectrum of HD 167756 with the GHRS during

[1] Based on observations obtained with the NASA/ESA *Hubble Space Telescope* through the Space Telescope Science Institute, which is operated by the Association for Research in Astronomy, Inc., under NASA contract NAS5-26555.

[2] Washburn Observatory, University of Wisconsin–Madison, 475 North Charter Street, Madison, WI 53706.

[3] Current address: Astronomy and Astrophysics, Villanova University, Villanova, PA 19085.

[4] Center for Space Research, Massachusetts Institute of Technology, Cambridge, MA 02139.

1991 June, shortly before the failure of the power supply on side 1. The observations were obtained with HD 167756 positioned in the small (0".25 × 0".25) science aperature. Details regarding the characteristics of the GHRS can be found in Duncan & Ebbets (1989). The exposures were acquired using step-pattern 6, which corresponds to two samples per diode. Observations at each primary wavelength consisted of exposures utilizing the FP-SPLIT = 4 procedure to reduce the effects of fixed-pattern noise present in the digicon detectors. This procedure consists of breaking each observation into a set of four subexposures, each obtained at a slightly different grating carousel position. For any single observation, individual subexposures (i.e. integrations ending in a data readout) were kept to approximately 5 minutes or less.

We followed the data reduction procedure of Cardelli et al. (1991) and Savage, Cardelli, & Sofia (1992) for data extraction, background processing and subtraction, and wavelength calibration of the data. The basic raw data reduction was performed using the package CALHRS at the GHRS computing facility at the Goddard Space Flight Center (CALHRS is also part of the standard Space Telescope Science Institute pipeline and IRAF reduction packages). This includes conversion to count rates, correcting for particle radiation, dark counts, diode nonuniformities, paired pulse events (where applicable), and wavelength calibration using the standard calibration tables available at the Space Telescope Science Institute as of 1992 May 15. The final data reduction, which included background subtraction and merging of the individual FP-SPLIT subexposures, was performed using software developed and tested at the University of Wisconsin–Madison. A second-order scattered light correction was applied according to the prescription outlined in Cardelli, Ebbets, & Savage (1990, 1993). The merged data have a resolution of approximately 3.5 km s^{-1} (FWHM) and S/N ≈ 20–35. Examples of the reduced spectra, plotted as observed count rates versus wavelengths, are shown in Figure 1. In Figure 1*a*, we show a portion of the Ech-A spectrum in the region of the Mg II doublet along with the fitted continuum. Figure 1*b* shows examples of the Ech-B spectra in the region of the two Zn II lines along with the continuum fits. Absorption from the interstellar lines occurs near the core of rotationally broadened stellar features ($v \sin i > 100$ km s^{-1}). Basic information about the observations including observed species, line rest wavelengths, *f*-values, and measured equivalent widths can be in Table 1.

To bring the interstellar absorption lines into a common velocity system, we employed a velocity "bootstrap" similar to the one prepared for the ξ Per sight line by Cardelli et al. (1991). The procedure is based upon the use of lines of the same species that occur in different observations to tie all other lines present in these observations into a common reference frame. In the absence of lines of the same species, the procedure defaults to lines of neutral species and lines from different species exhibiting similar levels of depletion. For our data, the lines of Zn II λλ2026, 2062 were used to tie Cr II λλ2062, 2066 and Mg I λ2026, which occur in the same observations, into a common reference system. Mg I λ2026 was subsequently used to tie in S I λ1807 and Si II λ1808. The wings of Si II λ1808 were used to tie in Si II λ1304 and the accompanying O I λ1302 line. Si II λ1304, O I λ1302, and Fe II λ2374 show a strong isolated feature at $v_{lsr} \approx 52$ km s^{-1} that was used to tie them together. Finally, since there were no useful low ion reference lines in the observation containing the Mg II doublet at λ1239/1240, these lines were aligned to those of Cr II which exhibit similar profiles. An additional velocity shift was applied to bring the "bootstrapped" velocity system into the heliocentric velocity frame found for Na I and Ca II ground-based observations of HD 167756 (Sembach, Danks, & Savage 1993). The high-velocity feature at +52 km s^{-1} (LSR) seen in O I λ1302, Si II λ1304, and Ca II λ3933 was used as a reference between the GHRS and ground-based data. The velocity shift applied to each observation is listed in Table 1. A final shift of +5.5 km s^{-1} was applied to all heliocentric velocities to bring them into the local standard of rest using the assumption of a solar neighborhood speed of +16.5 km s^{-1} in the direction $l = 53°$, $b = 25°$ (Mihalas & Binney 1981). We estimate that our corrected velocities are accurate to ±1 km s^{-1}.

The low-ion continuum-normalized profiles of Cr II λλ2062, 2066; Mg I λ2026; Mg II λλ1239, 1240; Zn II λλ2026, 2062; Si II λλ1808, 1304; and Fe II λ2374 are shown in Figures 2*a* and 2*b* plotted against LSR velocity. Figure 2*c* shows the absorption profiles of Ca II λ3993 and Na I λ5895 (Sembach et al. 1993). The resolutions of these data are about 5 km s^{-1} (FWHM). Also shown in Figure 2*c* are the H I 21 cm data of Danly et al. (1991) for the HD 167756 sight line where we have plotted antenna temperature as a function of LSR velocity. The H I data were obtained at the 140 foot (42.7 m) telescope at Green Bank with a velocity resolution of 1 km s^{-1} and a beam width of approximately 20′ (FWHM). Antenna side lobe con-

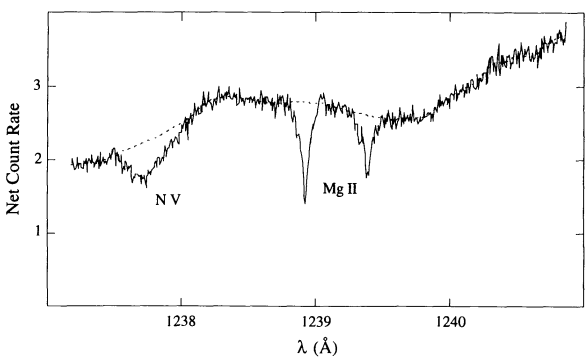

FIG. 1*a*

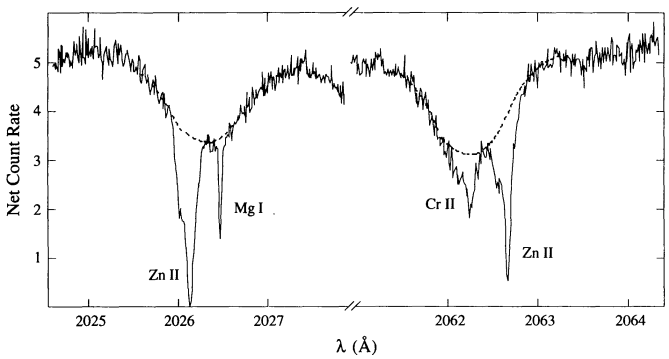

FIG. 1*b*

FIG. 1.—Portions of the echelle observations, plotted as net count rate in counts diode^{-1} s^{-1} for (*a*) Ech-A data in the region of 1239 Å and (*b*) Ech-B data in the region of 2026 and 2063 Å. Also shown are the fitted continua. The continuum fits in (*b*) corresponds to the stellar line profiles and were contrained by other stellar lines present in the data.

TABLE 1

NEUTRALS AND DOMINANT IONS OBSERVED TOWARD HD 167756[a]

Observation ID	Grating	Velocity Shift[b]	Species	λ_0 (Å)[c]	$\log f\lambda_0$[d]	W_λ ($\pm 1\ \sigma$)[e]
Z0JA010LM	ECH-A45	+2.2	Mg II	1239.925	0.171[f]	42.5 (2.3)
			Mg II	1240.395	−0.130[f]	23.4 (2.1)
Z0JA010IM	ECH-A43[g]	+0.9	P II	1301.874	1.351	38.0 (2.6)
			O I	1302.169	1.804	380.7 (3.1)
			Si II	1304.370	2.050[h]	291.0 (3.0)
Z0JA010RT	ECH-B31	−1.7	S I	1807.311	2.301	4.6 (1.2)
			Si II	1808.013	0.576[h]	185.7 (3.3)
Z0JAO10UT	ECH-B28	−2.5	Zn II	2026.136	2.996[i]	168.8 (3.8)
			Mg I	2026.477	2.369	26.3 (2.7)
Z0JA010VT	ECH-B27	−1.2	Cr II	2062.234	2.206[i]	51.6 (4.0)
			Zn II	2062.664	2.723[i]	116.5 (4.7)
			Cr II	2066.161	2.027[i]	36.0 (4.3)
Z0JA010WT	ECH-B24	−1.0	Fe II	2374.461	1.826	411.2 (8.4)

[a] All observations obtained with the small (0.″25 × 0.″25) science aperture, a sampling of two substeps per diode (STEP-PATT = 6), and the command FP-SPLIT = 4 (see text).

[b] Velocity shift (in km s^{-1}) required to bring the spectra into the correct heliocentric velocity reference frame. An additional shift of +5.5 km s^{-1} is required to bring the heliocentric velocities into the local standard of rest velocity reference frame.

[c] Line rest (vacuum) wavelength from Morton 1991.

[d] Logarithm of the product of the f-value and rest wavelength. All values were taken from the compilation of Morton 1991, except where noted.

[e] Measured equivalent width in mÅ along with 1 σ measurement error. These measures do not include the component seen at +52 km s^{-1} (see Fig. 2*b*).

[f] f-values adopted from results of Cardelli et al. 1991 and Sofia, Cardelli, & Savage 1994—see text.

[g] These data are listed for completeness but are not used in the analysis. The P II is heavily contaminated by the wing of O I and O I and Si II lines are strongly saturated and are unusable over the velocity range discussed here.

[h] f-value taken from the lifetime measurement of Bergeson & Lawler 1993a.

[i] f-value taken from the lifetime measurements of Bergeson & Lawler 1993b.

tamination has not been removed from the data. The analysis below will emphasize the velocity range of -25 km s$^{-1} \leq v_{\rm lsr} < 30$ km s^{-1}. Absorption by low ions at larger velocities, including the +52 km s^{-1} feature, will be discussed in more detail in a future paper.

3. SIGHT LINE OVERVIEW

HD 167756 lies in the direction $l = 351.°5$, $b = -12.°3$. The star was classified B0.5 Ia by Garrison, Hiltner, & Schild (1969, 1977) on the basis of high-dispersion optical spectra. We have confirmed the optical spectroscopic classification by examining the ultraviolet spectrum of the star. Using the observed colors of the star ($V = 6.30$, $B-V = -0.13$; Schild, Garrison, & Hiltner 1993) and the intrinsic colors of Johnson (1966), we derive a color excess $E(B-V) = 0.09$. We calculate a spectroscopic distance $d = 4.0$ kpc assuming the Population I absolute magnitude system of Walborn (1972) and the reddening relation $A_V = 3.1\ E(B-V)$. At this distance, the star lies at a Galactic altitude $z = -0.85$ kpc. Approximately one-third of the HD 167756 sight line is confined to the Galactic plane ($|z| < 250$ pc). The sight line passes through the interstellar medium in the solar neighborhood as well as the more general environment of the Galactic disk (see also Savage et al. [1994] for an additional review of the sight line).

The effects of Galactic rotation in the direction of HD 167756 are modest over the 4 kpc path length to the star. The low latitude of the sight line minimizes the radial component of motions perpendicular to the Galactic plane. At a distance of 4 kpc, a gas parcel would have a galactocentric distance of 4.7 kpc and an expected line-of-sight velocity of -26 km s^{-1} according to the rotation curve of Clemens (1985), which assumes a solar galactocentric distance of 8.5 kpc and solar circular rotation speed of 220 km s^{-1}. The neutral gas species are thought to have density distributions away from the Galactic plane consisting of a confined and an extended component (Lockman 1984). Scale heights of 500 to more than 1000 pc are found for the extended components (Lockman 1984; Edgar & Savage 1989; Sembach 1992; Sembach & Danks 1994). Therefore, some diminution of the neutral gas probably occurs over the second half of the sight line.

The H I 21 cm emission data of Danly et al. (1991) for the HD 167756 sight line are shown in Figure 2*c*. The H I profile has a maximum intensity at $v = +5.5$ km s^{-1}. The peak emission may be associated with the cold ($T \sim 20$ K) H I cloud discussed by Riegel & Crutcher (1972). Their H I data show a strong component at +7 km s^{-1} and weaker components at +4 and 0 km s^{-1}. The cold cloud has an optical depth of about one as seen in H I absorption and extends in longitude from $l = 345°$ to 25°. The H I data of Riegel & Crutcher indicate that the cloud may be confined to low latitudes, $|b| < 6°$, but the Ca II K-line study of Rickard (1974) and the Na I and Ca II survey of Sembach (1992) indicate that the cloud may be less confined in latitude than previously thought. Over longitudes between $l = 349°$ and 356°, a discrete H I feature between $b = -10°$ and $-15°$ is clearly visible in the Leiden–Green Bank H I survey maps of Burton (1985) at these velocities. At longitudes outside this range the feature blends in with the more general contours of the H I distribution at low velocities. Rickard and Riegel & Crutcher estimate a cloud distance of about 900 pc. Given this distance, the HD 167756 sight line would intersect the cloud at $z \approx -190$ pc.

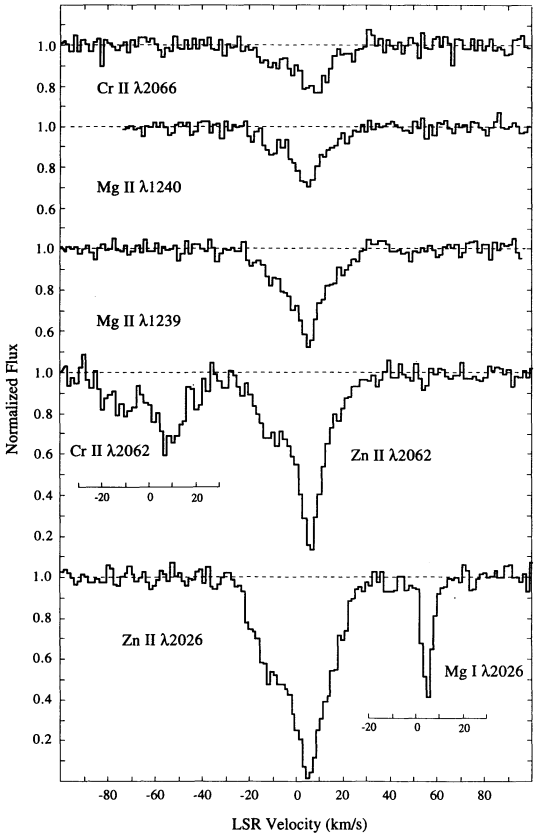

FIG. 2a

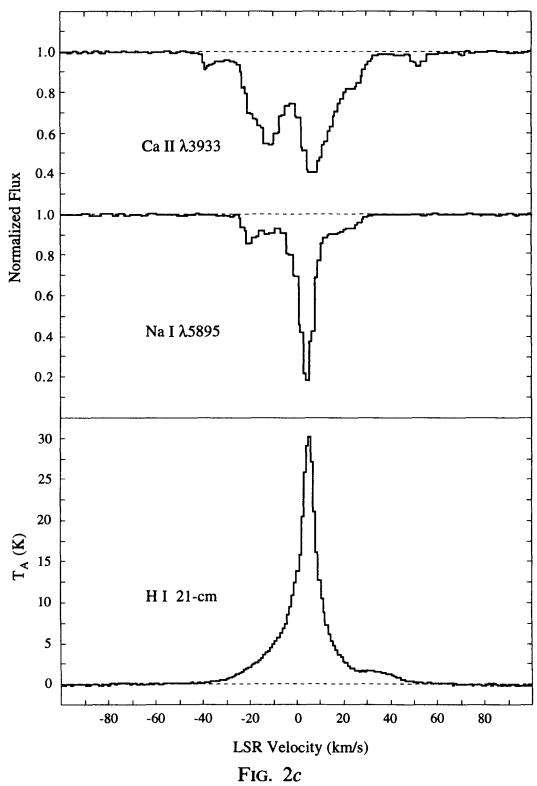

FIG. 2c

FIG. 2.—The continuum normalized line profiles, plotted against LSR velocity, are shown in (*a*) and (*b*) for the UV data obtained with the echelle gratings and in (*c*) for the optical Na I and Ca II along with the 21 cm H I emission profile.

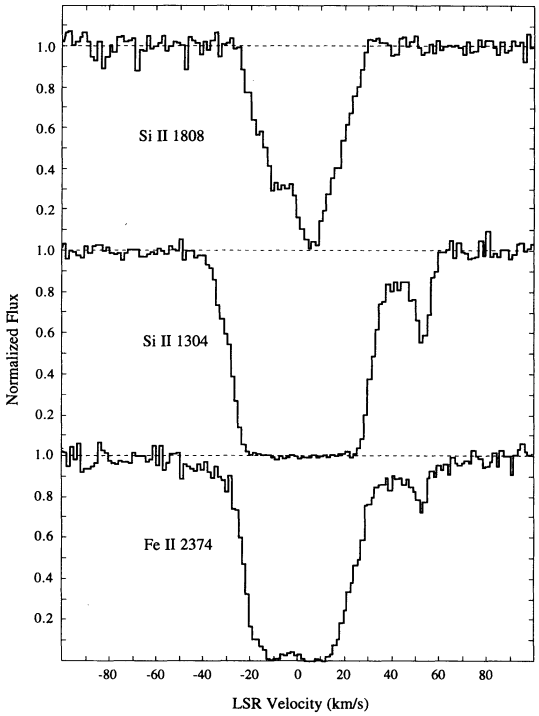

FIG. 2b

The overall structure of the H I profile shown in Figure 2*c* is rather complex. The positive velocity enhancement between +30 and +70 km s^{-1} is also present in the H I contour maps of Burton (1985). There is a general absence of absorption at these velocities in low ion profiles shown in Figures 2*a* and 2*b*, indicating that much of the emission may be coming from beyond the star. Both sets of H I data indicate that H I emission extends from −50 to +70 km s^{-1} in this direction. At small values of antenna temperature, antenna side lobe contamination may be responsible for the broad trailing wings seen in the H I profile shown in Figure 2*c*.

4. COLUMN DENSITIES VERSUS VELOCITY

The broad range of velocity ($\approx$60 km s^{-1}) exhibited by the observed low ion absorption toward HD 167756 in comparison to the instrumental resolution (3.5 km s^{-1}) provide us with an excellent opportunity to study the abundance and gas phase characteristics along the sight line. We choose to analyze the data by expressing the observed line profiles in the form of apparent optical depth profiles versus velocity (see Savage & Sembach 1991) which are defined as

$$\tau_a(v) = \ln [I_c(v)/I(v)] , \quad (1)$$

where $I(v)$ and $I_c(v)$ are the observed line intensity and the fitted continuum at v, respectively. From equation (1), the velocity-dependent apparent column density per unit velocity, $N_a(v)$, taken the form

$$N_a(v) = [\tau_a(v)/f\lambda] m_e c/\pi e^2$$
$$= [\tau_a(v)/f\lambda] 3.768 \times 10^{14} \text{ cm}^{-2} (\text{km s}^{-1})^{-1} , \quad (2)$$

where f is the line oscillator strength and λ is the line rest wavelength (in units of Å). In the limit where the line profile is completely resolved, equation (2) expresses the *true* column density distribution *independent of the degree of saturation.*

However, at 3.5 km s^{-1} resolution, the possible presence of narrow (unresolved) components in the data can give rise to *unresolved* saturated structure which can seriously distort the apparent column density profiles and lead to an underestimate of total column density over the affected velocity range. The presence of *unresolved* saturated structure can be explored by comparing two or more $N_a(v)$ profiles of the same species, whose $f\lambda$ are reasonably different (e.g., $\geq$factor 2). When unresolved saturated structure is present, the two profiles diverge from each other over the saturated region (see Savage & Sembach 1991), with the stronger line exhibiting lower values of $N_a(v)$. In this case, the stronger line, and possibly also the weaker line, underestimates $N_a(v)$.

An example of such a comparison is shown in Figure 3 where we plot log $N_a(v)$ for Zn II $\lambda\lambda$2026, 2062 for which $\Delta \log f\lambda = 0.3$ dex. The uncertainties shown for each profile are derived from a quadrature addition to the point-to-point statistical uncertainty, continuum fitting uncertainty, and an uncertainty associated with the scattered light correction (see Cardelli et al. 1993). (For a more detailed discussion of the error analysis, see §§ 3.3 and 3.4 of Savage et al. 1992.) An examination of Figure 3 shows that within the errors, both profiles agree quite well at all velocities indicating no *unresolved* saturated structure. The maximum apparent optical depth reached by the stronger of the two lines is $\tau_a(v)_{max} \approx$ 3.5–4. The absence of unresolved saturated structure at such large values of $\tau_a(v)_{max}$ is consistent with the presence of warm and possibly turbulent gas. Consider for comparison the GHRS echelle data of the atomic absorption in the -15 km s^{-1} component toward ζ Oph for which the effects of unresolved saturated structure become apparent for $\tau_a(v) \geq 0.2$ (Savage et al. 1992). If components like those typically associated with cold gas ($T < 100$ K) are present along the HD 167756 sight line, they are either weak or significantly broadened by turbulence. The implications of resolving the data to such large optical depths will be discussed further in § 6.

We can use the results of Figure 3 to conclude that the data for Mg II and Cr II do not contain unresolved saturated structure since $\tau_a(v)_{max} < 3$ in for both species. For Si II λ1808, a few points in the line core (i.e. $+2$ km $s^{-1} \leq v_{lsr} \leq +8$ km s^{-1}) exceed $\tau_a(v) \approx 3.5$, and so we suspect the possible presence of unresolved saturated structure. The same is true for Fe II λ2374 for the region $+2$ km $s^{-1} \leq v_{lsr} \leq +11$ km s^{-1} and for one or two points near $v_{lsr} \approx -11$ km s^{-1}. The $N_a(v)$ values in the affected regions should consequently be considered lower limits.

The log $N_a(v)$ profiles for the data analyzed here are shown in Figure 4. The errors follow from the discussion above. The value of the vertical scale for each species is shown on the left axis, with the separation of the tick marks corresponding to 0.2 dex. For Zn II, Cr II, and Mg II for which we have two lines each, the data were obtained by combining the individual $N_a(v)$ profiles. For Si II and Fe II, the data that we believe are affected by unresolved saturated structure are plotted as open symbols. We also show the $N_a(v)$ profiles for Na I λ5895 and Ca II λ3933. For Na I data, the open symbols correspond to data that are affected by unresolved saturated structure, which was assessed from a comparison between the λ5895 and λ5889 lines. For the Na I lines, which have about the same resolution as the UV data, we found that unresolved saturated structure becomes important for $\tau_a(v) > 1.4$. Although this is considerably smaller

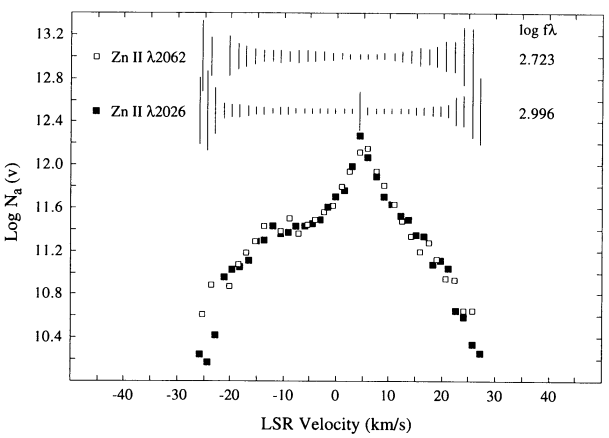

FIG. 3.—A comparison between the logarithm of the apparent column density profiles, $N_a(v)$ [cm^{-2} ($km\ s^{-1}$)$^{-1}$], for the pair of Zn II lines. The two $N_a(v)$ profiles agree quite well over the entire velocity range indicating that we are resolving the data even in the deep cores of the lines near $v_{lsr} \approx 5$ km s^{-1} (see Fig. 2*a*). The apparent optical depth at the core of the strongest line is at about 4. Resolving the data to such a large apparent optical depth suggests that the profile is dominated by warm gas ($T > 1000$ K) and possibly some cooler gas that is turbulently broadened.

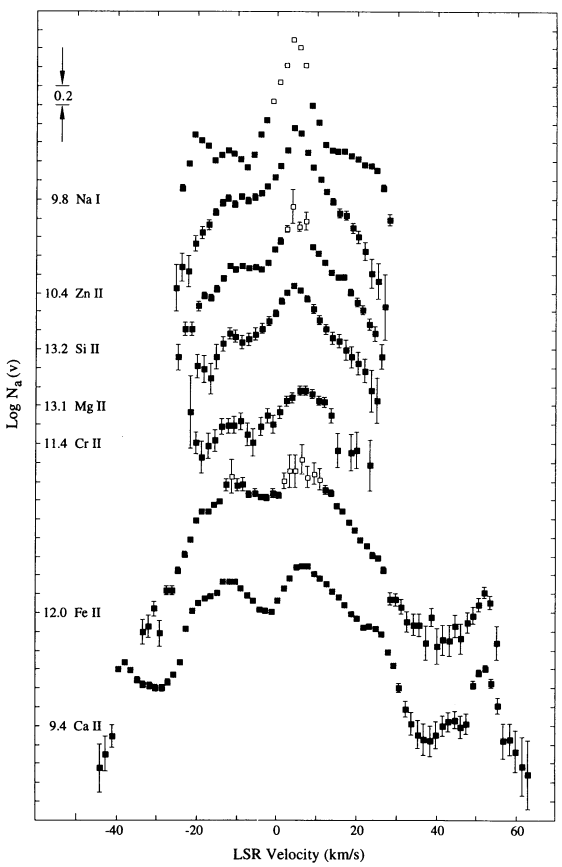

FIG. 4.—The logarithm of the apparent column density profiles, $N_a(v)$ [cm^{-2} ($km\ s^{-1}$)$^{-1}$], for the principal species observed toward HD 167756. The values listed along the left axis give the log $N_a(v)$ value and reference tick mark for each profile. The open symbols for Na I, Si II, and Fe II represent portions of the line profile where unresolved saturated structure occurs (see § 4). As such, the apparent column density corresponds to a lower limit.

than the value found for Zn II, it is still much larger than values found in cold clouds and suggests the presence of cool gas. The implications of this will be discussed further in § 6. For Ca II, $\tau_a(v) < 1$ at all velocities. Because the resolution of the Ca II data is about the same as for the UV data, we believe that no *unresolved* saturated structure is present.

The values of $\log f\lambda$ used to derive the $N_a(v)$ for the UV lines are given in Table 1. With the exception of Mg II, Si II, Cr II, and Zn II, the f-values, including those for Na I and Ca II, were taken from the compilation of Morton (1991). For Zn II and Cr II, we adopt the experimental results of Bergeson & Lawler (1993a). For Si II λ1808, we adopt the recent experimental measure of Bergeson & Lawler (1993b). For the weak Mg II doublet, our adopted $\log f\lambda$ corresponds to an increase of about 0.67 dex (see Cardelli et al. 1991 and Sofia, Cardelli, & Savage 1994) over the value listed by Morton (1991) which was taken from Hibbert et al. (1983).

While our main goal is to make maximum use of the information provided through the velocity-dependent apparent column densities, there are good reasons for producing integrated column densities as well. For example, since we are probing absorption through local and relatively low density interarm disk gas, integrated column densities can supply a fiducial measure for the Galaxy to which QSO absorption lines studies probing external galaxies can be compared. This is particularly true of species like Zn and Cr which serve as probes of metallicity and gas depletion onto dust in other disk systems (Meyer & Roth 1990). The result of integrating $N_a(v)$ along with errors are given in Table 2 for the total profile as well as for three distinct LSR velocity regions. The principal core, centered near $v_{\rm lsr} \approx +5$ km s^{-1}, constitutes the dominant "diffuse cloud(s)" in the sight line and contains between 70% (first ions) and 85% (neutrals) of the total column density while the $|v_{\rm lsr}| > 10$ km s^{-1} gas contains between 15% (neutrals) and 30% (first ions) of the total column density.

5. RELATIVE ABUNDANCES

5.1. *Terminology*

We define the velocity-dependent *normalized gas phase elemental abundance* of species X, relative to hydrogen, as

$$A(v)_{\rm X/H} = \log [N(v)_{\rm X}/N(v)_{\rm H}] - \log (N_{\rm X}/N_{\rm H})_{\odot} , \quad (3)$$

where $(N_{\rm X}/N_{\rm H})_{\odot}$ is the solar or cosmic reference abundance (e.g., Anders & Grevesse 1989) to which the gas phase abundance $N(v)_{\rm X}/N(v)_{\rm H}$ is normalized. Since we are using the apparent optical depth method, we derive $A(v)_{\rm X/H}$ through a ratio of $N_a(v)$ profiles. Such an approach has been employed elsewhere (Joseph & Jenkins 1991; Sembach & Savage 1992; Sembach et al. 1993) and produces as meaningful a result as is found in cases where profile fitting can also be performed (Sembach 1992; Spitzer & Fitzpatrick 1993). In the ISM literature, equation (3) is often referred to as a measure of *depletion onto dust*. However, we find this designation to be confusing since what equation (3) actually species is the *fractional abundance of species* X, normalized to solar, that is *present in the gas phase*. We shall therefore refer to $A(v)_{\rm X/H}$ as the normalized gas phase abundance, with negative values of $A(v)_{\rm X/H}$ (i.e., less-than-solar abundances) referred to as being underabundant.

5.2. *Velocity Dependence*

In order to preserve the velocity information available in our data, use of equation (3) requires that we use $N(v)_{\rm H}$ derived from the H I 21 cm profile [T_b(K) was transformed to $N(v)$ in units of cm^{-2} (km s^{-1})$^{-1}$ using the optically thin approximation, $N(v) = 1.823 \times 10^{18} T_b(v)$ from Spitzer (1978)]. Figure 5 shows the $A(v)_{\rm Zn/H}$ derived from the ratio of $N_a(v)_{\rm Zn}$ to $N(v)_{\rm H\,I}$. The GHRS data have been averaged over two data samples (e.g., one diode). The H I data have been smoothed and resampled to the same effective resolution. Between -20 km s$^{-1} \le v_{\rm lsr} \le 20$ km s^{-1}, $\langle A(v)_{\rm Zn/H} \rangle \approx -0.28$ with maximum

TABLE 2

INTEGRATED COLUMN DENSITIES

Species	Number of Lines	log N ($\pm 1\ \sigma$)[a] A[b]	B[c]	C[d]	Total	$[{\rm X/H}]_{\odot}$[e]	$A_{\rm X/H}$[f]
Mg I[g]	1	11.99 (0.19)	12.89 (0.03)	11.60 (0.32)	12.96 (0.04)	...	...
Mg II	2	14.76 (0.05)	15.31 (0.02)	14.48 (0.08)	15.47 (0.02)	−4.41	−0.93
Si II	1	15.16 (0.01)	>15.67[h]	14.76 (0.02)	>15.83[h]	−4.45	>−0.53
Cr II	2	12.71 (0.06)	13.09 (0.03)	12.21 (0.15)	13.28 (0.03)	−6.32	−1.21
Fe II	1	>14.48[h]	>14.70[h]	13.94 (0.01)	>14.95[h]	−4.49	>−1.37
Zn II	2	12.55 (0.02)	13.12 (0.01)	12.09 (0.03)	13.25 (0.01)	−7.35	−0.22
Na I[g]	2	11.56 (0.01)	12.48 (0.01)[i]	11.31 (0.01)	12.55 (0.01)	...	...
Ca II[g]	1	12.08 (0.01)	12.26 (0.01)	11.69 (0.01)	12.55 (0.01)	...	...

[a] Results of integrating the apparent column densities, $N_a(v)$ as shown in Fig. 4, over the velocity regions as defined below. The error in log N, $\sigma_{\log N}$ ($= 0.43\sigma_N/N$), derive from the integration and include the point-to-point statistical uncertainty, continuum fitting uncertainty, and the uncertainty in the scattered light correction (see Cardelli, Ebbets, & Savage 1993).

[b] Region A corresponds to absorption over the range -25 km s$^{-1} \le v_{\rm lsr} \le -5$ km s^{-1}.

[c] Region B corresponds to absorption over the range -5 km s$^{-1} \le v_{\rm lsr} \le 15$ km s^{-1}.

[d] Region C corresponds to absorption over the range 15 km s$^{-1} \le v_{\rm lsr} \le 30$ km s^{-1}.

[e] Logarithm of the cosmic (meteoritic) abundances from Anders & Grevesse 1989.

[f] Logarithm of the gas phase abundance of X relative to hydrogen normalized to the cosmic abundance from Anders & Grevesse 1989 as in eq. (3). The total H I column density toward HD 167756, derived from the damping wings of Lyα (Diplas & Savage 1994a, b) is log N(H I) = 20.81.

[g] Represent trace ionization state.

[h] Velocity range contains some amount of *unresolved* saturated structure for which the integrated column density represents a lower limit. With the exception of the CORE of Fe II, the column density is probably underestimated by no more than 20%–30% (0.08–0.12 dex).

[i] Corrected for unresolved saturated structure using the results of Savage & Sembach 1991. The total column density is in excellent agreement with that determined by Sembach 1992 using both the apparent optical depth method and profile fitting.

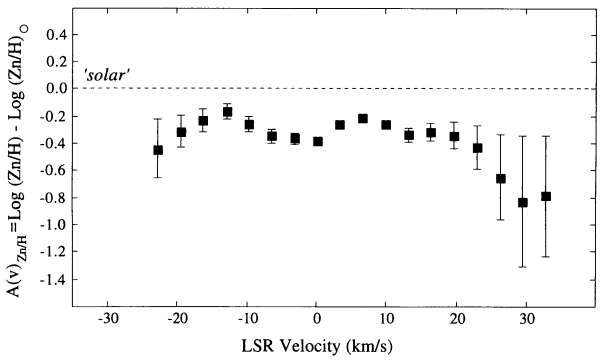

FIG. 5.—The logarithm of the relative abundance of Zn, Zn/H, normalized to cosmic abundance (from Anders & Grevesse 1989), $A(v)_{Zn/H}$, as a function of LSR velocity. The data were derived from the ratio of the Zn $N_a(v)$ profile (Fig. 4), binned over two data samples, to the 21 cm H I profile from Fig. 2*c* converted to column density (see § 5.2). The data appear very smooth and we consider these data to be consistent with a more or less constant value of $A(v)_{Zn/H}$ with velocity, a reasonable conclusion considering the potential spatial sampling incompatibility between the extremely small solid stellar angle for the absorption measurement and the broad antenna beam of the emission measurement. The mean value of $A(v)_{Zn/H}$ derived from the data are within 15% of the mean value derived from the ratio of the integrated Zn profile and H I derived from the Lyα absorption profile (Diplas & Savage 1994a, b). Since Zn is the dominant ionization state, these data represent the total gas phase abundance of Zn. The data indicate that Zn is only mildly depleted onto grains.

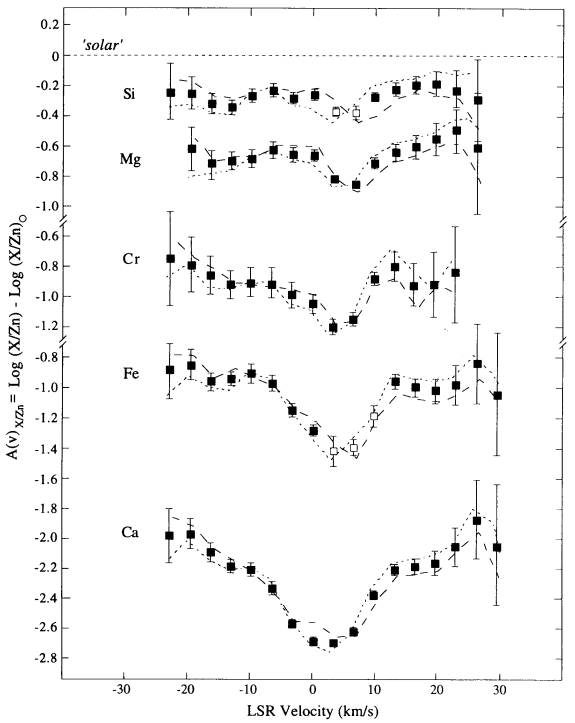

FIG. 6.—The logarithm of the relative abundance of species X, X/Zn, normalized to cosmic abundance (from Anders & Grevesse 1989), $A(v)_{X/Zn}$, as a function of LSR velocity for data of Si II, Mg II, Cr II, Fe II, and Ca II (see § 5.2). For all species except Ca, these data represent the dominant ionization state and should therefore represent the total gas phase abundance. As in Fig. 5, the data have been binned over two data samples. The open symbols for Si II and Fe II correspond to the data where unresolved saturated structure is present and should be considered lower limits. The short-dashed and long-dashed lines are the corresponding values of $A(v)_{X/Zn}$ derived assuming a ± 1 km s^{-1} velocity registration uncertainty between species X and Zn. These data can be converted to $A(v)_{X/H}$ by adding $A(v)_{Zn/H} \approx -0.22$, derived from the integrated N(Zn) and N(H I) from Diplas & Savage (1994a, b). Despite the fact that Ca II is a trace ionization state, it appears to trace the velocity dependence of $A_{Fe/Zn}$ quite well, suggesting a smooth and nearly constant degree of ionization.

variations of about $\pm 25\%$. This mean value compares quite well with the value $A_{ZN/H} \approx -0.22$ derived from the integrated Zn column density (Table 2) and log $N_{H\,I} = 20.81$ derived from the damping wings of Lyα (Diplas & Savage 1994a, b). However, because the H I $N(v)$ data are derived from an *emission line* obtained with a 20′ beam and have not been corrected for side lobe contamination, much of this variation may be due to a general incompatibility of this data with our line-of-sight *absorption-line* measures. For example, the decrease in $A(v)_{Zn/H}$ for $v_{lsr} > 20$ km s^{-1} is the result of the broad, weak H I emission component seen at this velocity (Fig. 2*c*), which probably arises from more spatially distributed gas or emission from beyond the star. Furthermore, the "bump" in $A(v)_{Zn/H}$ around $v_{lsr} \approx +5$ km s^{-1} may be the result of saturation in $N(v)_H$ at the line core.

As an alternative to using the H I emission-line data, we can represent the normalized abundances relative to some species like Zn by replacing $N(v)_H$ in equation (3) with $N(v)_{Zn}$. We choose Zn for this purpose because it is a more compatible tracer of the neutral gas (with respect to the other observed species) than the 21 cm emission data. Also, its gas phase abundance is generally not much different from solar (see Jenkins 1987), and from Figure 5, it seems reasonable to assume that $A(v)_{Zn/H} \approx$ constant within the uncertainties inherent in the comparison to radio H I measures. Zn is also a useful choice since the abundances of Cr and Fe relative to Zn appear to be independent of variations in the bulk metal abundance, [Fe/H] $\equiv$ log (Fe/H)/log (Fe/H)$_\odot$, among stars of different populations (Wheeler, Sneden, & Truran 1989). (Although [X/H] and $A_{X/H}$ carry the same meaning, we use separate designations to distinguish between stellar and interstellar measures.) We shall refer to the normalized gas phase abundance of species X in this form as $A(v)_{X/Zn}$. Figure 6 shows $A(v)_{X/Zn}$ for Si, Mg, Cr, Fe, and Ca. As in Figure 5, the measurements have been averaged over two data samples. The open symbols for Si and Fe represent data which are affected by some degree of unresolved saturated structure, and so these data are lower limits. The long-dashed and short-dashed lines correspond to $A(v)_{X/Zn}$ derived from applying to ± 1 km s^{-1} uncertainty in the velocity alignment of the $N_a(v)$ profiles.

Relative to Zn, all species represented in Figure 6 exhibit some level of underabundance relative to solar over the entire velocity range, with the largest underabundance occurring in the principal absorbing component near $v_{lsr} \approx 5$ km s^{-1}. Possible sources of and contributions to these underabundances are discussed below.

5.2.1. *Ionization*

Although the data shown in Figures 5 and 6 are derived from only a single ionization state, namely X^+, it can be shown that in gas dominated by neutral hydrogen, H^0, X^+ dominates all other ionization states for the species represented here, and so X^+/H^0 or X^+/Y^+ are good measures of the total gas phase abundance. (The exception to this is Ca II with an I.P. < 13.6 eV.) However, if ionized gas (H^+) is present in the sight line where the relative contributions of X^+ and H^0 (or Zn^+) are determined by the ionization structure, the data shown in Figures 5 and 6 may deviate from the true gas phase abundances. With one possible exception (see Savage et al. 1994), the

sight line to HD 167756 does not pass near H II regions associated with hot stars. However, in long path-length sight lines, especially those sampling halo gas, some contributions from low-density photoionized gas is expected as indicated by observations of faint optical emission lines and pulsar dispersion measures (Reynolds 1991, 1992 and references therein). The ionized gas is associated with regions of warm H^+ characteristic of low-excitation H II regions (Reynolds 1993). Direct evidence for ionized gas in the sight line toward HD 167756 can be found in intermediate resolution GHRS spectra showing strong absorption from species like Si III λ1206 as well as lower column density contributions from Si IV (Savage et al. 1994) over the entire velocity range considered here.

We proceed by assuming that the sight line consists of some physically separate combination of both strictly *neutral* (X^+ and H^0) and partially *ionized* (i.e., containing X^+, X^{++}, H^0, and H^+) gas and assess the impact this has on the observed quantities (X^+/H^0 or X^+/Zn^+) by accounting for the higher ionization states (X^{++} and H^+) *in the ionized gas.* We borrow from the standard terminology used in interstellar cloud chemistry, $x(X) = N(X)/N(H)$, where $N(X) = N(X^0) + N(X^+) + N(X^{++})$ and $N(H) = N(H^0) + N(H^+)$ are the total column densities of X and H, respectively. We ignore the possible presence of H_2 but show in § 6 that along the sightline to HD 167756, $f(H_2) \equiv 2N(H_2)/[2N(H_2) + N(\text{H I})] < 0.1$. Letting the subscripts *i*, *n*, and *all*, refer to the various species in the (partially) ionized gas, neutral gas, and *all* the gas, respectively, it follows that

$$x(X^+)_i = N(X^+)_i/N(H)_i$$
$$x(X^{++})_i = N(X^{++})_i/N(H)_i$$
$$x(H^+)_i = N(H^+)_i/N(H)_i \, .$$

These quantities represent the fractional amount of these species present in the (partially) ionized gas portion of the sight line column *only*. With regards to the full gas column, we also introduce

$$x(H^+)_{all} = N(H^+)_i/N(H)_{all} = N(H^+)_i/[N(H)_n + N(H)_i]$$
$$F(H) = N(H)_i N(H)_{all} = N(H)_i/[N(H)_n + N(H)_i] \, ,$$

where $x(H^+)_{all}$ represent the ratio of H^+ to total, H, and $F(H)$ represents the fraction of the total gas column containing (partially) ionized gas. The quantities $x(H^+)_i$, $x(H^+)_{all}$, and $F(H)$, which are related through $x(H^+)_{all} = x(H^+)_i F(H)$, will be particularly important in the discussions that follow. Note that the observations refer to the existence of a species *in all the gas* and therefore relate to quantities with the subscript *all*.

To proceed, we employ the steady state photoionization models of low-density, diffuse gas of Domgörgen & Mathis (1994). The model results used here represent volume-averaged quantities and correspond to a range of excitation parameters (i.e., photon/electron densities), with the lowest excitation parameter being the one that fits the observed spectrum of the Reynolds Layer (see Domgörgen & Mathis 1994). For Si, Mg, Fe, Cr, and Zn, the models (J. Mathis, private communication) indicates that the photoionized diffuse gas consists almost entirely of the first and second ionization stages (X^+ and X^{++}) with the relative contributions depending upon the ionization, $x(H^+)_i$. The models also indicate that the values of the relative ionization of X, $x(X^{++})_i/x(X^+)_i$, for our species are bracketed by those of Si and Fe, with Si yielding the smallest values of $x(X^{++})_i/x(X^+)_i$ for an arbitrary value of $x(H^+)_i$.

The impact that ionized gas has on the *observed quantities* will depend upon the value of both the fractional amount of ionized gas in the column, $F(H)$, and the degree to which this gas is ionized, $x(H^+)_i$. From the lower dispersion Si III data, we find $Si^+/Si^{++} \approx 20$–30 for $v_{lsr} < -10$ km s^{-1} and $v_{lsr} > +15$ km s^{-1}. Unfortunately, for $-10 \leq v_{lsr} \leq 15$ km s^{-1}, the Si III profile is very strong and may contain significant unresolved saturated structure so we can only supply an upper limit of $Si^+/Si^{++} < 200$. Consequently, the discussion below can only be directly applied to the gas outside the velocity range from -10 to 15 km s^{-1}.

For a particular value of all of H^+ to total H in the column, $x(H^+)_{all}$, the quantities $x(H^+)_i$ and $F(H)$ are coupled such that large $x(H^+)_i$ corresponds to small $F(H)$ and vice versa [recall that $x(H^+)_{all} = x(H^+)_i F(H)$]. From the models we find that the observed quantity $Si^+/Si^{++} \approx 20$–30, $x(H^+)_{all}$ ranges from about 0.2 to 0.4 for fractional ionization of $0.9 \geq x(H^+)_i \geq 0.4$. For $Si^+/Si^{++} \approx 50$, we find $x(H^+)_{all}$ ranges from 0.1 to 0.3 for $0.9 \geq x(H^+)_i \geq 0.3$. [We note that the above results include the limit where $F(H) \approx 1$ (i.e., there is no strictly neutral gas—the entire column consists of partially ionized gas), analogous to the clouds toward HD 93521 (Spitzer & Fitzpatrick 1993). This limit is particularly relevant to the assessment of the physical conditions in the sight line and the implications will be discussed later.] From the analysis of the distribution of pulsar dispersion measures in the Galaxy by Reynolds (1991), we can estimate the "expected" total column density of H^+ along the line of sight to HD 167756. Using this estimate and $N(H^0) = 6.5 \times 10^{20}$ cm^{-2} from Diplas & Savage (1994a, b), we find $x(H^+)_{all} \approx 0.24$, in excellent agreement with the range of values found above.

Adopting $x(H^+)_{all} \approx 0.2$–0.3, we can determine the impact of ionized gas on the "observed" abundances from the ionization models for a (coupled) range of $x(H^+)_i$ and $F(H)$. For abundances measured relative to hydrogen (i.e., Fig. 5), we find the following results. For $F(H) > 0.8$ and $x(H^+)_i < 0.4$ (i.e., the gas column consists mostly of partially ionized gas but at a low fractional ionization), the apparent abundances will be overestimated by about +0.14 dex for all species. For $F(H) < 0.3$ and $x(H^+)_i > 0.9$ (i.e., the gas column consists mostly of strictly neutral gas but with the partially ionized gas showing high fractional ionization), the apparent abundances will be overestimated by as little as +0.06 dex (Fe) to as much as +0.12 dex (Si). For abundances measured relative to Zn (i.e., Fig. 6), these overestimations are considerably smaller being <0.01 for the low fractional ionization case and <0.05 for the high fractional ionization case for all species. These smaller values result from the fact that for a significant range of fractional ionization, $x(H^+)_i$, the quantity $x(X^{++})_i/x(Zn^{++})_i$ is typically within a factor 2 of unity while $x(X^{++})_i$ and/or $x(Zn^{++})_i$ exhibit a large range of variation.

The above results were formulated by assuming that there is no difference in the intrinsic abundance of X between the neutral and ionized gas. Such differences can arise if, for example, a larger fraction of the neutral gas is locked up in dust [this does not apply to the limit where the gas is fully ionized or $F(H) \approx 1$]. However, even if the difference in the intrinsic abundances between the neutral and partially ionized as is as large as 0.5 dex, the impact of ionized as on the measured abundances is not significantly different from what was found above.

Based on the above analysis, we conclude that to within the uncertainty limits of $x(H^+)_{all}$, the presence of ionized gas con-

tributes, on average, only a minor influence (≤ 0.1 dex) on abundances derived from the observable quantities (i.e., X^+/H^0), at least for $|v_{lsr}| > 15$ km s^{-1}, and so the data in Figure 5 and especially Figure 6 are good representations of the "true" gas phase abundances for this velocity range. This conclusion depends little upon variations in the fractional ionization, $x(X^+)_i$, or the relative amount of ionized gas, $F(H)$, as long as $x(H^+)_{all}$ is held constant. Unfortunately, for $|v_{lsr}| \leq 15$ km s^{-1}, we cannot independently confirm values for $x(H^+)_{all}$. However, the relatively small variation of $A(v)_{Zn/H}$ in Figure 5 suggests that contributions from ionized gas in this velocity range are not substantially different from those inferred for the high velocity gas.

5.2.2. *Variations in Intrinsic Abundances*

In our presentation of the normalized abundances, we have used the solar systems abundances of Anders & Grevesse (1989) as the reference cosmic abundance. While these solar system abundances carry a quoted internal uncertainty of 10%–20%, it is not unreasonable to question whether larger uncertainties apply or even if the use of these data as reference abundances is valid for gas residing over large Galactic distances. For example, Geis & Lambert (1992) and Kilian (1992) explored elemental abundances toward early B stars and found that relative to solar, the abundances of C and O are systematically *lower* by as much as 0.2–0.4 dex, the abundance of Fe is higher by about 0.2 dex, and Si is at or near solar. Similar results for C and O have also been suggested for Orion Nebula abundances (see references in Table 12 of Geis & Lambert 1992), although Walter, Dufor, & Hester (1992) argue that incorporating temperature fluctuations in the nebula can result in near solar values. In any case, we must consider that variations in the intrinsic elemental abundances may contribute to the abundance variations seen in Figure 6 since our sight line probes gas in the inner Galaxy where the effects of Galactic abundance gradients may be present (see Rana 1991 for a general review).

It is interesting to note that the elements we discuss here can be conveniently divided into two groups, namely elements produced by the α-process (Na, Mg, Si, and Ca) and "Fe-peak" elements (Cr, Fe, and Zn). For stellar metal abundances of $+0.3 > [Fe/H] \geq -2$, there is strong observational evidence that $\langle [Cr/Fe] \rangle \approx \langle [Zn/Fe] \rangle \approx 0$ (Wheeler et al. 1989 and references therein). However, for the same range of [Fe/H], the α-process elements range from $0 \leq \langle [\alpha/Fe] \rangle \leq +0.35$ (Gratton & Sneden 1987). Our choice to derive abundances relative to Zn suggests that if intrinsic abundance variations exist in our sight line, they may be particularly evident in the comparison of Mg/Zn and Si/Zn to Cr/Zn and Fe/Zn.

Although the scatter is considerable, stellar abundance measurements suggest that [Fe/H] increases by perhaps +0.02 to +0.1 dex per kpc toward the Galactic center from the Sun (see Rana 1991). Unfortunately, such measures for the other elements discussed here are poorly represented. However, if we assume that variations in [Fe/H] are traced by variations in [Zn/H] and the absorption for -26 km s$^{-1} \leq v_{lsr} \leq 0$ km s^{-1} traces the 4 kpc for HD 167756, the $A(v)_{Zn/H}$ data in Figure 5 indicate no significant systematic increase since the observed variations from the mean abundance could well be the result of either ionization effects (see § 5.3.2 above) or the incompatibility of comparing the 21 cm emission data. The absence of a significant gradient in our data is also supported by the lack of variation with velocity of the Si abundance data (relative to Zn) if we assume that [Si/Fe] should also show some variation with [Fe/H]. However, we acknowledge that our negative velocity data may in fact not trace the entire 4 kpc because of the density stratification of the gas away from the Galactic plane. Also, Galactic rotation is only expected to carry the gas out to $v_{lsr} \approx -26$ km s^{-1}, and so gas at this velocity may be the result of random cloud motions of ± 10 km s^{-1}. Consequently, the lack of an observed gradient in our data may be the result of the gas being well mixed in velocity or a lack of sufficient sampling of inner Galaxy gas, or both.

The (questionable) lack of definitive evidence for an abundance gradient for $v_{lsr} \leq 0$ km s^{-1} does not exclude the possibility of general variations in the intrinsic abundances somewhere along the sight line. In fact, there is evidence that shows that for nearby disk stars formed at the same epoch as the Sun, there is a spread in the measured Fe abundance of $0 \geq [Fe/H] \geq -0.5$ dex (Edvardsson et al. 1993). However, we believe that the effects of such variations in our data must be minor for the following reasons. First, the abundance of Si relative to Zn is constant over the entire velocity range to better than ± 0.1 dex. To within the errors, this is also true for Mg, Cr, and Fe for $|v_{lsr}| > 10$ km s^{-1}. This is particularly significant if we attribute the negative and positive velocity absorption to gas arising from distinct regions somewhere along the 4 kpc to the star. Second, the overall abundances relative to Zn, especially the intercomparison between different species as a function of v_{lsr}, are completely consistent with what is typically observed in low density, warm gas, including examples for relatively nearby sight lines (see Table 3 and § 5.2.3). We therefore conclude that there is little or no evidence for variations in the intrinsic abundances in this sight line. The likely source of the observed abundance differences from solar values is discussed below.

5.2.3. *The Effects of Dust*

Based upon the results of §§ 5.2.1 and 5.2.2, we are left to conclude that the major source of the less-than-cosmic abundances seen in Figure 6 is the result of the effects of gas depletion onto dust. This conclusion is strengthened by the fact that the observed abundances are consistent with what is typically seen in warm diffuse gas. Table 3 lists the values of $\langle A(v)_{X/Zn} \rangle$ for HD 167756 in the $|v_{lsr}| \geq 10$ km s^{-1} gas and at $v_{lsr} \approx +5$ km s^{-1}. Also listed are abundance data for specific diffuse gas components in a selected sample of sight lines for which the data have also been obtained with the GHRS echelles. These include μ Col Components A (-10 km s$^{-1} \leq v_{lsr} \leq +10$ km s^{-1}; Sofia, Savage, & Cardelli 1993), ζ Oph Component A ($v_{lsr} \approx -13$ km s^{-1}; Savage et al. 1992), and an average of two low velocity components ($v_{lsr} \approx +4$ km s^{-1} and $+9$ km s^{-1}) toward HD 93521 (Spitzer & Fitzpatrick 1993). All the literature data for Si, Mg, and Cr were adjusted for the f-values adopted here. For HD 93521, no data for Zn are available, and so we used $A_{Zn/H} \approx -0.22$ derived from the HD 167756 data, a value consistent with warm, low-density diffuse gas (Jenkins 1987). An important similarity between these different components is that at the resolution of the GHRS echelles, they all show a lack of unresolved saturated structure for $2 \leq \tau_a(v)_{max} \leq 4$. These $\tau_a(v)_{max}$ values are a factor of 10 or more larger than those observed in cold clouds (e.g. $T < 100$ K) like those seen at low velocity toward ζ Oph (i.e., Component B; Savage et al. 1992) and suggest the presence of warm, turbulent gas. The distances to these stars are also listed in the table and put an upper limit on the distance to the absorbing gas. For

TABLE 3

NORMALIZED ABUNDANCES RELATIVE TO Zn FOR EXAMPLES OF WARM, DIFFUSE GAS

SIGHT LINE	d (kpc)	$\tau_a(v)_{max}$ [b]	$A_{X/Zn}$ [a] Si	Mg	Cr	Fe
HD 167756 ($v_{lsr} \approx +5$)	4.0	3.5	> -0.38	-0.82	-1.18	> -1.40
μ Col (Component A)[c]	1.1	2.2[b]	-0.33	...	-1.14	-1.26
ζ Oph (Component A)[d]	0.1	2.5[b]	...	-0.85	-1.09	-1.35
HD 167756 ($v_{lsr} \leq -10$).....	4.0	4.0	-0.30	-0.65	-0.86	-0.92
HD 167756 ($v_{lsr} \geq +10$).....	4.0	4.0	-0.25	-0.58	-0.88	-0.98
HD 93521 ($\langle v_{lsr} \rangle \approx +6.5$)[e].....	1.7	1.9[b]	-0.28	-0.63	...	-1.01

[a] Normalized gas phase abundances measured relative to Zn: $A_{X/Zn} = \log [N_X/N_{Zn}) - \log [N_X/N_{Zn}]_\odot$. Literature data for Si, Mg, and Cr have been adjusted to the f-values adopted here.

[b] Maximum apparent optical depth reached to which there is no unresolved saturated structure. For the sight lines indicated, $\tau_a(v)_{max}$ represents the largest values found from the data but do not necessarily represent the largest values possible.

[c] μ Col Component A (-10 km s^{-1} $< v_{lsr} <$ $+10$ km s^{-1}) data taken from Sofia, Savage, & Cardelli 1993. Typical 1 σ error in $A_{X/Zn}$ corresponds to ± 0.05 dex.

[d] ζ Oph Component A ($v_{lsr} \approx -13$ km s^{-1}) data taken obtained from Savage, Cardelli, & Sofia 1992. Typical 1 σ error in $A_{X/Zn}$ corresponds to ± 0.03 dex.

[e] With $b = +62°$, HD 93521 resides 1.5 kpc above the Galactic disk, and so the sight line predominantly samples halo gas. The data are taken from Spitzer & Fitzpatrick 1993 and correspond to the average of the two components located at $v_{lsr} \approx +4$ and $+9$ km s^{-1}. These authors did not observe the Zn lines, and so we use the normalized Zn abundance relative to hydrogen found for HD 167756, $A_{Zn/H} \approx -0.22$, a value characteristic of warm diffuse gas (Jenkins 1987). Typical 1 σ error in $A_{X/Zn}$ corresponds to about ± 0.03 dex.

HD 93521, $b = +62°$ and therefore the sight line predominantly samples halo gas.

The data in the table have been segregated into two groups based upon bulk abundance characteristics. The normalized abundances within each group are remarkably similar, while between the two groups there are noticeable differences for Fe and Cr. We believe this similarity supports the contention that the observed abundances arise from the effects of gas depletion onto dust, especially considering the diverse range of directions and distances. It is difficult to imagine that significant intrinsic abundance variations are present and are somehow exactly compensated by depletion and/or ionization effects.

Although the sample shown in Table 3 is limited, the relative abundances within each group and particularly the element-to-element differences between each group are a benchmark of depletion characteristics. For example, the differences between the two groups are similar to those seen in the relationship between measured gas phase abundances and mean sight line density (Jenkins 1987). In addition, these differences are consistent with the important results of Joseph (1988) who found that as the abundance of one species changes, all species on average show changes in the same sense (e.g., increase or decrease). Also, on average, the magnitude of these changes tend to scale with the relative depletion, with more highly depleted species like Fe and Cr showing larger changes than more lightly depleted species like Si and Zn. This behavior is seen not only in the data in Table 3, but also in the comparison between the individual components observed toward ζ Oph (Savage et al. 1992), μ Col (Sofia et al. 1993), HD 93521 (Spitzer & Fitzpatrick 1993), and the $A(v)_{X/Zn}$ data for HD 167756 (see also Sofia et al. 1994). We see no evidence that the obsrved velocity-dependent normalized abundances toward HD 167756 are the result of anything other than the predictable effects of gas depletion onto dust.

6. PHYSICAL CONDITIONS ALONG THE SIGHT LINE

In addition to the high-resolution echelle data, we also obtained some data with the intermediate resolution (12 km s^{-1}) grating G140M. In one observation (ID = Z0JA0116M), moderately strong absorption from Cl I λ1347 is present, yielding log $N \approx 13.0$ ($W_\lambda \approx 21$ mÅ) derived from a direct integration of the apparent column density profile assuming $f = 0.153$ (Schectman et al. 1993) and no line saturation. The abundance of Cl I in diffuse clouds is strongly influenced by reactions between Cl II and H_2. This reaction leads to HCl^+ (Jura 1974) from which Cl I can result through several channels (Jura & York 1978 and references therein). A comparison of N(Cl I) and $N(H_2)$ for sight lines with $E(B-V) < 0.13$ from Jenkins et al. (1986) shows a modest correlation from which we find $17.5 < \log N(H_2) < 19.5$ and $10^{-3} < f(H_2) \equiv 2N(H_2)/[2N(H_2) + N(H\ I)] < 10^{-1}$ for the sight line to HD 167756. These values are similar to those of low density diffuse molecular clouds (see Jenkins et al. 1986).

In our analysis of the UV absorption lines using the apparent optical depth method (see § 4), we found that the cores of the Zn II profiles were resolved to apparent optical depth values as large as 3.5–4. For the core of the optical Na I absorption, the maximum apparent optical depths to which the data are resolved (1.4) are smaller than for Zn II but are still significantly larger than the values derived from GHRS echelle data of ζ Oph, a sight line through a cold ($T < 100$ K), diffuse molecular cloud. To explore the implications of resolving the data to such large apparent optical depths, we conducted profile-fitting simulations which were constrained by these apparent optical depth limits. We found that in the absence of turbulent broadening [i.e., the component(s) width is determined solely by the thermal broadening], very little cold gas can be present in the sight line to HD 167756 since modest amounts of such gas leads to unresolved saturated structure at apparent optical depths much smaller than what is observed. We found that if we added turbulent motions to the velocity field, a modest amount of cold gas could be present. However, hiding too much cold gas becomes somewhat unrealistic since it requires that the gas be highly fragmented into many weak, cold components present in a very narrow velocity width in the core of the absorption (the cores of the observed data restricts us to total velocity broadening—thermal plus turbulent—of no larger than 2.5 km s^{-1}).

While it is likely that the gas in the sight line to HD 167756 is turbulent and probably contains some cold gas, the sight line is likely dominated by warm gas. For the gas-containing dominant ions like Zn II, our simulations suggest the mean temperature is likely in excess of 1000 K. For neutral species like Na I, for which unresolved saturated structure becomes present at smaller apparent optical depths, the mean temperature is probably of the order of 500–1000 K. Further limits on the gas temperature are discussed below.

The presence of both neutral and dominant ion species in the data set allow us to explore the sight line characteristics through the ionization equilibrium equation

$$n_i/n_{i+1} = \alpha_{i+1} n_e/\Gamma_i \,, \tag{4}$$

where n_i and n_{i+1} are the volume densities of some arbitrary species in the i and $i+1$ ionization state, respectively, α_{i+1} is the volume recombination rate (cm^3 s^{-1}), n_e is the electron density, and Γ_i is the photoionization rate (s^{-1}) from the i to $i+1$ state. In our application of equation (4), we replace the volume densities with observed apparent column densities (e.g., Fig. 4) from which we can explore the velocity dependence of the ionization structure. Specifically, we explore the velocity dependence of the ionization using Na I. Using Zn II as a substitute for Na II, equation (4) can be written as

$$\alpha_{\rm Na\ II} n_e/\Gamma_{\rm Na\ I} = N({\rm Na\ I})/N({\rm Na\ II}) \approx N({\rm Na\ I})/N({\rm Zn\ II}) \times C_1 \,, \tag{5}$$

where C_1 (≈ 0.04) is equal to the ratio of the gas phase abundance of Zn II relative to Na II and we assume $N_{\rm Na\ II}/N_{\rm H} \approx (N_{\rm Na}/N_{\rm H})_\odot\, 10^{(A_{\rm Na/H})}$. We have adopted $A_{\rm Na/H} \approx -0.6$, the value characteristic of warm, diffuse gas (Jenkins 1987) and assumed that like Zn, $A_{\rm Na/H}$ shows no dependence with velocity (see Fig. 5; the implications of assuming $A_{\rm Na/H} \approx 0$ are discussed below).

The logarithm of equation (5) is shown plotted in Figure 7 using the velocity-dependent apparent column density ratios for the term N(Na I)/N(Zn II). The open square symbols are lower limits corresponding to the portion of the Na I data affected by unresolved saturated structure. Also plotted as half-filled diamonds are the data derived from the observed Mg I and Mg II apparent column density profiles, scaled to equation (5) using

$$\alpha_{\rm Na\ II} n_e/\Gamma_{\rm Na\ I} = N({\rm Mg\ I})/N({\rm Mg\ II}) \times C_2 \approx (\alpha_{\rm Mg\ II} n_e/\Gamma_{\rm Mg\ I}) \times C_2 \,, \tag{6}$$

where $C_2 = (\alpha_{\rm Na\ II}/\alpha_{\rm Mg\ II})(\Gamma_{\rm Mg\ I}/\Gamma_{\rm Na\ I}) \approx 4.3$. The values for α and Γ are taken from Pequignot & Aldrovandi (1986) and extrapolted for $T > 1000$ K (see also Aldrovandi & Pequignot 1973, 1974). Although α and Γ can be highly dependent on local physical conditions, this has little effect on equation (6) since the ratios of these quantities are rather insensitive to changes in either the radiation field or temperature (for example, for $T \leq 4000$ K, $\alpha_{\rm Na\ II}/\alpha_{\rm Mg\ II}$ varies by at most 10%).

The relatively good agreement in Figure 7 between the results of equations (5) and (6) allows us to put additional limits on the temperature of the gas. For $T > 4000$ K, dielectronic recombination figures predominantly in the production of Mg I while having no influence on Na I. Relative to $T < 4000$ K, $\alpha_{\rm Na\ II}/\alpha_{\rm Mg\ II}$ for $T \approx 7000$ K decreases by about a factor 3 (-0.5 dex). The lack of any significant difference between the Na and Mg results suggests that the mean temperature of the gas does not exceed 5000 K, provided that Na is depleted. Combining this with the discussion above implies that the gas containing the dominant ions is likely characterized by 1000 K $< T <$ 5000 K.

If we assume that α/Γ is constant with velocity, the data in Figure 7 indicate that the electron density varies by up to a factor of 10 across the various absorbing components in the sight line, with nearly identical maximum values near $v_{\rm lsr} \approx -20$, 0, and $+25$ km s^{-1}. Assuming that the radiation field is typical of the diffuse ISM and the gas has a uniform temperature of 3000 K, we find $0.02 \leq n_e \leq 0.2$ cm^{-3}. This range of n_e is strikingly similar to the range of values found from the fine structure excitation of C II (C II*) in the clouds toward the halo star HD 93521 (Spitzer & Fitzpatrick 1993), a warm gas sight line with similar gas phase abundances.

If the electrons come only from carbon, the results found here suggest unrealistically large densities (up to nearly 10^3 cm^{-3}), values more characteristic of denser molecule-bearing environments with substantially larger gas depletion onto dust than is indicated by any of the HD 167756 data. It is possible that our adopted value of $A_{\rm Na/H} \approx -0.6$ is too small. If we assume a solar gas phase abundance for Na (i.e., no Na depletion, $A_{\rm Na/H} = 0$), this shifts the data in Figure 7 derived from equation (5) down by about 0.6 dex (a factor of 4). The offset this produces relative to the results derived from the Mg data (eq. [6]) suggests the presence of dielectronic recombination. To bring the results from equation (6) back into agreement requires a gas temperature of about 7000 K, a result we cannot necessarily discount. However, adopting these changes results in at most a factor of 2 decrease in the n_e values. The only obvious way to substantially lower the n_e values would be to increase $\alpha_{\rm Na\ II}$ by significantly lowering the gas temperature. However, based upon our analysis of the apparent optical depth profiles and the discussion above, this does not seem possible.

The most likely explanation for such large n_e values is that the neutral gas contains some amount of ionized hydrogen. This explanation is significant in light of the results for

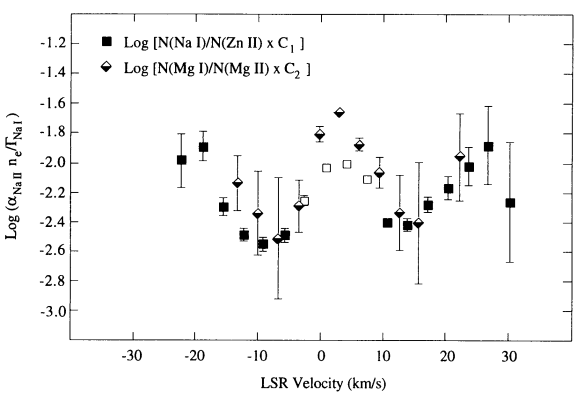

FIG. 7.—Ionization equilibrium for Na, log ($\alpha_{\rm Na\ II} n_e/\Gamma_{\rm Na\ I}$), plotted against LSR velocity. In the absence of Na II data, we have used N(Zn II) so that N(Na I)/N(Na II) $\approx N$(Na I)/N(Zn II) $\times C_1$, where C_1 (≈ 0.04) is equal to the ratio of the gas phase abundance of Zn II relative to Na II assuming $N_{\rm Na\ II}/N_{\rm H} \approx (N_{\rm Na}/N_{\rm H})_\odot\, 10^{(A_{\rm Na/H})}$ and $A_{\rm Na/H} \approx -0.6$. The open symbols correspond to the portion of the Na I profile affected by unresolved saturated structure and as such are lower limits. The half-filled symbols represent the equivalent values of log ($\alpha_{\rm Na\ II} n_e/\Gamma_{\rm Na\ I}$) derived from a scaling of the ionization equilibrium of Mg, N(Mg I)/N(Mg II) $\times C_2$, where $C_2 = (\alpha_{\rm Na\ II}/\alpha_{\rm Mg\ II})(\Gamma_{\rm Mg\ I}/\Gamma_{\rm Na\ I}) \approx 4.3$. Assuming $\alpha/\Gamma \approx$ constant with velocity, the data suggest large variations in the electron density along the sight line.

HD 93521 presented by Spitzer & Fitzpatrick (1993) who argued that electrons associated with the ionized hydrogen were coexistent with the neutral atomic gas, a result that puts severe constraints on the mechanism(s) responsible for the ionization. However, there are some significant differences from the HD 93521 sight line that suggest that the ionized and neutral gas toward HD 167756 are only partially mixed.

Our analysis of the apparent optical depth profiles along with the data in Figure 7 indicates that the mean gas temperature is likely smaller than in the HD 93521 sight line and what is typically inferred for the warm neutral medium ($\approx 10^4$ K; McKee & Ostriker 1977). We also find evidence indicating that trace species like Na I arise in gas at lower mean temperatures than the dominant ions like Zn II. Also, since Ca II is ionized with photons less energetic than 13.6 eV, it is expected to be a trace ionization state, especially in warm, low density. Assuming $A_{Ca/H} \approx A_{Fe/H}$ for warm clouds (Jenkins 1987), Spitzer & Fitzpatrick (1993) used the observed $A_{Ca\ II/H}$ to derive N(Ca III) for the HD 93521 clouds. From ionization equilibrium, they found n_e values in general agreement with what was derived from C II* data. We applied the same approach for our data and show the results in Figure 8. Assuming $T \approx 3000$ K and taking $\Gamma_{Ca\ II}$ from Pequignot & Aldrovandi (1986) and $\alpha_{Ca\ III}$ from Shull & Van Steenberg (1982), we find $0.04 \leq n_e \leq 0.1$ cm^{-3}, somewhat lower than the result from Figure 7 but not inconsistent considering the uncertainties in both α and Γ. However, a comparison between Figures 7 and 8 show that the overall pattern is significantly different. Furthermore, the results for Ca indicates the lowest electron densities occur in the principal absorbing components near $v_{lsr} \approx 0$ km s^{-1}. The inconsistencies between Figures 7 and 8 suggest that Ca II is tracing a more extended and perhaps more uniform component(s), separate from the gas being traced by Na I and Zn II (see Sembach & Danks 1994 for a more general discussion of the relationship between Na I and Ca II along low-density sight lines).

A plausible explanation for the differences seen in the neutral gas species is that the absorption is tracing a series of interfaces or transition zones between the neutral and ionized gas having $x(H^+)_{all} \approx 0.2$–0.3. The peaks in the N(Na I)/N(Zn II) ratio shown in Figure 7 occur at velocities near the structured components seen in higher ionization stages such as Si IV and C IV.

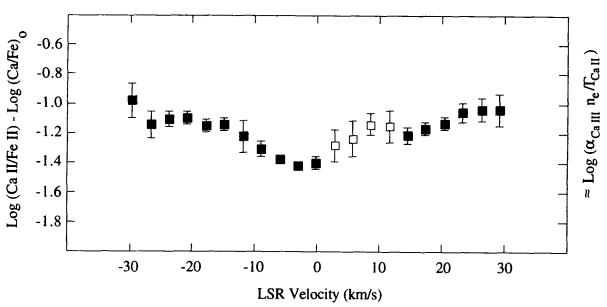

FIG. 8.—Ionization equilibrium for Ca, log ($\alpha_{Ca\ III}$ $n_e/\Gamma_{Ca\ II}$), plotted against LSR velocity. These data were derived assuming $A(v)_{Ca/H} \approx A(v)_{Fe/H}$ in warm, diffuse gas (Jenkins 1987), a technique employed by Spitzer & Fitzpatrick (1993) to produce convincing results for the data of HD 93521. From this, it is straightforward to show that $A(v)_{Ca\ II/Zn} - A(v)_{Fe/Zn} \approx \log (\alpha_{Ca\ III}\, n_e/\Gamma_{Ca\ II})$ for the HD 167756 data. Unlike in Fig. 7, the results derived for Ca are very smoothly varying and appear completely inconsistent with the results derived for both Na and Mg. This suggests that gas influencing the ionization equilibrium of Ca is distinctly different from and more uniform than the gas probed by the data in Fig. 7.

Savage Sembach, & Cardelli (1994) concluded that the constancy of the N(C IV)/N(Si IV) ratios and the line widths of the higher ionization components are compatible with an origin in conductive interfaces between warm ($T \approx 10^4$ K) and hot ($T \approx 10^6$) gas. The neutral and highly ionized gases cannot be well mixed due to the higher temperatures ($\approx 10^5$ K) required to create species such as Si IV and C IV by collisional ionization. Therefore, we may be seeing the effects of a temperature and density gradient in the absorption lines of species that arise (at least partially) within the transition zones between the neutral and highly ionized gases.

7. SUMMARY

1. We present high-resolution (3.5 km s^{-1}) GHRS measurements of the Mg II, Si II, Cr II, Fe II, and Zn II lines toward HD 167756, a low-latitude halo star at a distance of 4 kpc in the direction $l = 351°.5$, $b = -12°.3$ and a Galactic altitude of $z = -0.85$ kpc. The data have S/N ≈ 30. Supplemental Na I, Ca II, and H I data are also presented for comparison with the UV lines.

2. We convert the observed absorption line data into measures of the apparent column density per unit velocity, $N_a(v)$, over the velocity range $-25 < v_{lsr} < +30$ km s^{-1} for each species observed. We find that, with the exception of the absorption at the cores of the Na I λ5895, Si II λ1808, and Fe II λ2374 lines, there is no unresolved saturated structure in the lines.

3. A comparison of the $N_a(v)$ profile for Zn II with the 21 cm $N(v)$ profile for H I shows that the gas phase abundance of Zn relative to the solar abundance, $A(v)_{Zn/H}$, is relatively constant between -25 and $+35$ km s^{-1}, with a mean value of -0.28 dex. This compares quite well with the value of -0.22 dex derived from a comparison between the integrated Zn II $N_a(v)$ and N(H I) obtained from the Lyα absorption profile.

4. We use the $N_a(v)$ profiles to construct ratios of Mg II, Si II, Cr II, Fe II, and Ca II relative to Zn II, normalized to solar abundances, as a function of velocity. We show that, compared to Zn, the other species show an underabundance relative to their solar values, with the largest underabundances occurring in the $v_{lsr} \approx 5$ km s^{-1} component(s), for which we find logarithmic abundances $A_{Si/Zn} > -0.38$, $A_{Mg/Zn} = -0.82$, $A_{Cr/Zn} = -1.18$, and $A_{Fe/Zn} > -1.40$ dex.

5. We show that ionization effects, abundance gradients, or intrinsic abundance variability cannot be significant sources for the underabundances observed. The underabundances are most likely the result of gas phase depletion of elements onto dust grains. Comparisons with the gas phase abundances along other diffuse, warm gas sight lines, like the halo sight line to HD 93521, support this interpretation to do the derived physical properties of the sight line.

6. From a comparison of the observed Si II profile and Si III (G160M) profile, we conclude $Si^+/Si^{++} = 20$–30 for $v_{lsr} < -10$ km s^{-1} and $v_{lsr} > +15$ km s^{-1}. Using photoionization models, this ratio implies a total fractional abundance of ionized hydrogen of 0.2–0.4, which is in excellent agreement with the value of 0.24 we find if we compare the observed neutral hydrogen column density along the sight line to estimates of $N(H^+)$ from the distribution of electron densities from pulsar dispersion measures (Reynolds 1991).

7. We show that the HD 167756 sight line is a low-density, diffuse sight line based upon the observed line strengths and supporting data for species such as Cl I. If we assume that Na

is modestly depleted, the gas temperatures of the neutral regions giving rise to the observed absorption are between 1000 and 5000 K, although some clouds particularly those detected in Na I, may have $T < 1000$ K. However, if Na is not depleted, the gas temperature could be as large as 7000 K. The electron densities determined from ionization balance considerations are $0.02 < n_e < 0.20$ cm^{-3}. Such high values, which are more typical of denser molecule-bearing clouds, probably signify some mixing between strictly neutral gas and gas containing H^+.

8. Differences arising in the physical properties like temperature and electron density determined from species such as Na I or Zn II and Ca II can be explained if some of the low ion absorption occurs in transition regions between neutral and ionized gas. Structured absorption seen in more highly ionized species such as Si IV and C IV (Savage, Sembach, & Cardelli 1994) favors the existence of such regions along the sight line.

We would like to acknowledge many useful discussions with Derck Massa, John Mathis, Todd Tripp, and U. J. Sofia. We also would like to thank the referee for useful comments and remarks. The data reduction and analysis were performed at the Midwest Astronomical Data Analysis Facility (MADRAF) at the University of Wisconsin–Madison. J. A. C. acknowledges support from NASA-LTSARP grant NAGW-2520. K. R. S. acknowledges support from a Hubble Fellowship provided the NASA through grant HF-1038.101-92A from the Space Telescope Science Institute, operated by AURA, Inc. under NASA contract NAS5-26555. B. D. S. acknowledges support from NASA grant NAG5-1852.

REFERENCES

Aldrovandi, S. M. V., & Péquignot, D. 1973, A&A, 25, 137
———. 1974, Rev. Brasileira de Fisica, 4, 491
Anders, E., & Grevesse, N. 1989, Geochem. Cosmochem. Acta, 53, 197
Bergeson, S. D., & Lawler, J. E. 1993a, ApJ, 414, L137
———. 1993b, ApJ, 408, 382
Burton, W. B. 1985, A&AS, 62, 365
Cardelli, J. A., Ebbets, D. C., & Savage, B. D. 1990, ApJ, 365, 789
———. 1993, ApJ, 413, 401
Cardelli, J. A., Savage, B. D., Bruhweiler, F. C., Smith, A. M., Ebbets, D. C., Sembach, K. R., & Sofia, U. J. 1991, ApJ, 377, L57
Clemens, D. P. 1985, ApJ, 295, 422
Danly, L., Lockman, F. J., Meade, M. R., & Savage, B. D. 1991, ApJS, 81, 125
Diplas, A., & Savage, B. D. 1994a, ApJ, 427, 474
———. 1994b, ApJS, 93, 211
Domgörgen, H., & Mathis, J. S. 1994, ApJ, 428, 647
Duncan, D. K., & Ebbets, D. C. 1989, Goddard High Resolution Spectrograph Instrument Handbook, Space Telescope Science Institute
Edgar, R. J., & Savage, B. D. 1989, ApJ, 240, 762
Edvardsson, B., Andersen, J., Gustafsson, B., Lambert, D. L., Nissen, P. E., & Tomkin, J. 1993, A&A, 275, 101
Garrison, R. F., Hiltner, W. A., & Schild, R. E. 1969, ApJ, 157, 313
———. 1977, ApJS, 35, 111
Geis, D. R., & Lambert, D. L. 1992, ApJ, 387, 673
Gratton, R. G., & Sneden, C. 1987, A&A, 178, 179
Hibbert, A., Dufton, P. L., Murray, M. J., & York, D. G. 1983, MNRAS, 205, 535
Jenkins, E. B. 1987, in Interstellar Processes, ed. D. J. Hollenbach & H. A. Thronson (Dordrecht: Reidel), 533
Jenkins, E. L., Savage, B. D., & Spitzer, L. 1986, ApJ, 301, 355
Johnson, H. L. 1966, ARA&A, 4, 193
Joseph, C. L. 1988, ApJ, 335, 157
Joseph, C. L., & Jenkins, E. B. 1991, ApJ, 368, 201
Jura, M. 1974, ApJ, 190, L33
Jura, M., & York, D. 1978, ApJ, 219, 861
Kilian, J. 1992, A&A, 262, 171
Lockman, F. J. 1984, ApJ, 283, 90
McKee, C. F., & Ostriker, J. P. 1977, ApJ, 218, 148
Meyer, D. M., & Roth, K. C. 1990, ApJ, 363, 57
Mihalas, D., & Binney, J. 1981, Galactic Astronomy (2d ed.; New York: W. H. Freeman & Co.)
Morton, D. C. 1991, ApJS, 77, 119
Péquignot, D., & Aldrovandi, S. M. V. 1986, A&A, 161, 169
Rana, N. C. 1991, ARA&A, 29, 129
Reynolds, R. J. 1991, in The Interstellar Disk-Halo Connection in Galaxies, ed. H. Bloemen (Dordrecht: Kluwer), 67
———. 1992, ApJ, 392, L35
———. 1993, in Massive Stars: Their Lives in the Interstellar Medium, ed. J. P. Cassinelli & E. B. Churwell (ASP Conf. Ser., 35), 338
Rickard, J. J. 1974, A&A, 31, 47
Riegel, R. W., & Crutcher, R. M. 1972, A&A, 18, 55
Savage, B. D., Cardelli, J. A., & Sofia, U. J. 1992, ApJ, 401, 706
Savage, B. D., & Sembach, K. R. 1991, ApJ, 379, 245
Savage, B. D., Sembach, K. F., & Cardelli, J. A. 1994, ApJ, 420, 183
Schectman, R. M., Federman, S. R., Beideck, D. J., & Ellis, D. G. 1993, ApJ, 406, 735
Schild, R. E., Garrison, R. F., & Hiltner, W. A. 1983, ApJS, 51, 321
Sembach, K. R. 1992, Ph.D. thesis, Univ. of Wisconsin
Sembach, K. R., & Danks, A. 1994, A&A, in press
Sembach, K. R., Danks, A., & Savage, B. D. 1993, A&AS, 100, 107
Sembach, K. R., & Savage, B. D. 1992, ApJS, 83, 147
Shull, J. M., & Van Steenberg, M. 1982, ApJS, 48, 95
Sofia, U. J., Cardelli, J. A., & Savage, B. D. 1994, ApJ, 430, 650
Sofia, U. J., Savage, B. D., & Cardelli, J. A. 1993, ApJ, 413, 251
Spitzer, L., Jr. 1978, Physical Processes in the Interstellar Medium (New York: Wiley), chap. 11
Spitzer, L., & Fitzpatrick, E. L. 1993, ApJ, 409, 299
Walborn, N. R. 1972, AJ, 77, 312
Walter, D. K., Dufour, R. J., & Hester, J. J. 1992, 397, 196
Wheeler, J. C., Sneden, C., & Truran, J. W. 1989, ARA&A, 27, 279